REPORT DOCUMENTATION PAGE

Form Approved
OMB No. 0704-0188

1. AGENCY USE ONLY (Leave blank)	2. REPORT DATE	3. REPORT TYPE AND DATES COVERED
	November 20, 1995	Final Technical 02/01/92–07/31/95

4. TITLE AND SUBTITLE
Segmentation of Multilook, Multifrequency, and Multipolarimetric SAR Data

5. FUNDING NUMBERS
F49620-92-J-0130

AFOSR-TR 96-0027

6. AUTHOR(S)
Rama Chellappa

7. PERFORMING ORGANIZATION NAME(S) AND ADDRESS(ES)
Department of Electrical Engineering
University of Maryland
College Park, MD 20742

8. PERFORMING ORGANIZATION REPORT NUMBER

9. SPONSORING/MONITORING AGENCY NAME(S) AND ADDRESS(ES)
Air Force Office of Scientific Research
110 Duncan Avenue, Suite B115
Bolling Air Force Base 20332

10. SPONSORING/MONITORING AGENCY REPORT NUMBER

11. SUPPLEMENTARY NOTES

12a. DISTRIBUTION/AVAILABILITY STATEMENT
Approved for public release.
Distribution unlimited.

12b. DISTRIBUTION CODE

13. ABSTRACT *(Maximum 200 words)*

This final report summarizes the findings of the research, "Segmentation of Multi-look, Multi-frequency and Multi-polarimetric SAR data" supported by the AFOSR contract F49620-92-J0130. During the duration of the project, we have developed algorithms for a) Markov Random Field based segmentation of high resolution SAR images, b) detection of man-made features in SAR images and c) labeling, as well as, grouping algorithms. These algorithms have been integrated to produce a 2-D site model of the given SAR image. The 2-D site model is an annotated description of the SAR image incorporating natural and man-made features such as trees, grass, water, open terrain, buildings, roads and shadows. Such site models are useful for delineating regions of interest (which serve as focus of attention mechanisms) and for providing local context in ATR algorithms.

14. SUBJECT TERMS
Segmentation of multi-polarimetric data, man-made feature extraction in high resolution SAR images, building wide area site models for SAR images

15. NUMBER OF PAGES
20

16. PRICE CODE

17. SECURITY CLASSIFICATION OF REPORT	18. SECURITY CLASSIFICATION OF THIS PAGE	19. SECURITY CLASSIFICATION OF ABSTRACT	20. LIMITATION OF ABSTRACT
UNCLASSIFIED	UNCLASSIFIED	UNCLASSIFIED	UL

1 Executive Summary

This final report summarizes the findings of the research, "Segmentation of Multi-look, Multi-frequency and Multi-polarimetric SAR data" supported by the AFOSR contract F49620-92-J0130. During the duration of the project, we have developed algorithms for a) Markov Random Field based segmentation of high resolution SAR images, b) detection of man-made features in SAR images and c) labeling, as well as, grouping algorithms. These algorithms have been integrated to produce a 2-D site model of the given SAR image. The 2-D site model is an annotated description of the SAR image incorporating natural and man-made features such as trees, grass, water, open terrain, buildings, roads and shadows. Such site models are useful for delineating regions of interest (which serve as focus of attention mechanisms) and for providing local context in ATR algorithms.

The 2-D site models will be useful for the urban clutter mitigation problem in the ATR domain. Target detection in SAR images of urban areas, with a low occurrence of false alarms, is a difficult problem because of the presence of a large number of spurious bright returns. These arise mainly due to the cardinal effects caused by the vertical walls/roofs of buildings, as well as due to other cultural objects which produce bright backscatter. Several of these false targets can be eliminated by the use of context-based arguments once we are able to segment and label the scene. Moreover, target detection algorithms can be cued to look on roads and clearings, once these have been delineated in the SAR image, resulting in computational savings. We have begun interactions with Dr. Les Novak of MIT Lincoln Laboratory on integrating the 2-D site models in their ATR algorithm. Another potential application of our work is in SAR seeker. All of our algorithms have been tested on the $1' \times 1'$ high resolution fully polarimetric SAR data collected at Lincoln Laboratory. We acknowledge the assistance of Dr. Les Novak in providing this data.

The research contract partially supported the Ph.D. thesis work of Mr. Shyam Kuttikkad. He is expected to graduate in December 1996.

Publications resulting from this contract are:

1. E. Rignot and R. Chellappa, " Segmentation of Polarimetric Synthetic Aperture Radar Data", IEEE Trans. Image Processing, Vol. IP-1, pp. 281-300, July 1992.

2. E. Rignot and R. Chellappa, "Maximum a posteriori Classification of Multifrequency, Multi-look Synthetic Aperture Radar Intensity Data", Jl. Optical Society of America, A, Vol. 10, pp. 573-582, April 1993.

3. S. Kuttikkad and R. Chellappa, "Non-Gaussian CFAR Techniques for Target Detection in High Resolution SAR Images", Proc. First Intl. Conf. on Image Processing, Austin, TX, pp. 910-914, Nov. 1994.

4. R. Chellappa, "Image Understanding and Statistics: What each can do for the other?" (Invited paper), Joint Statisticians Meeting, Toronto, August 1994.

5. S. Kuttikkad and R. Chellappa, "Building Wide area 2-D Site Models from High Resolution SAR Images", Intl. Symposium on Computer Vision, Coral Gables, FL. Nov. 1995.

2 Polarimetric Feature Vector Based Segmentation

In [5], Derin et. al. have presented stochastic models for single- and multi-look, intensity and complex, single polarization data, and developed maximum a posteriori segmentation algorithms for each case. Single polarization segmentation schemes do not completely account for the influence of targets and terrain on the polarization of the electromagnetic signal. In order to exploit all the polarization information, fully polarimetric methods have to be used. Fully polarimetric radars permit the measurement of the complete polarimetric scattering matrix of each resolution cell in the region being imaged. One common technique for the segmentation of fully polarimetric data involves the statistical modeling of the polarimetric measurement vector, followed by an estimation of the region labels.

The simplest model for the polarimetric complex data is the multivariate circular Gaussian distribution, which was considered in [12, 19]. This model allows for the easy specification of marginal densities and characterization of the statistical properties of the data in terms of first and second order moments, while providing simple closed form expressions for various estimates of the region labels. In [12] a maximum likelihood (ML) estimate was obtained for the region labels. A Markov Random Field (MRF) model was proposed in [19] to obtain a maximum a posteriori (MAP) estimate of the region labels, leading to a smoother segmentation.

Let $X_s = [HH, HV, VV]_s$ denote the single look polarimetric measurement vector at site s. The VH polarization term is not present because it is symmetrized with respect to HV during data calibration. Each component of X_s is a complex number of the form $HV = |HV| \exp\{i\phi_{HV}\}$. The conditional distribution of the polarimetric measurement vector X_s, given it's region label L_s, is assumed to be circular Gaussian :

$$p(X_s/L_s = l) = \frac{1}{\pi^3} exp\{-X_s^* C_l^{-1} X_s^T - log|C_l|\} \tag{1}$$

where $L_s (= l, l \in \{1, 2, \ldots, K\})$, is the set of region labels. Superscripts * and T denote conjugation and transposition respectively. $C_l =< X^{*T} X >_l$ is the 3×3 polarimetric covariance matrix, with $< >_l$ denoting ensemble averaging over the region l. The model of (1) assumes that each region has stationary backscatter statistics.

2.1 Maximum Likelihood Estimation of Region Labels

For azimuthally symmetric targets, which is the case of most natural targets, the cross-polarized return is uncorrelated with the two co-polarized returns, giving rise to the covariance matrix

$$C_l = \sigma_l \begin{pmatrix} 1 & 0 & \rho_l \sqrt{\gamma_l} \\ 0 & \epsilon_l & 0 \\ \rho_l^* \sqrt{\gamma_l} & 0 & \gamma_l \end{pmatrix} \tag{2}$$

where

$$\sigma_l =< |HH|^2 >_l; \qquad \epsilon_l = \frac{< |HV|^2 >_l}{< |HH|^2 >_l}$$
$$\gamma_l = \frac{< |VV|^2 >_l}{< |HH|^2 >_l}; \qquad \rho_l = \frac{< HHVV^* >_l}{\sqrt{< |HH|^2 >_l < |VV|^2 >_l}} \tag{3}$$

C_l can be inverted analytically and substituted in (1) to give

$$p(X_s/L_s = l) = \frac{1}{\pi^3}\exp\left\{-\frac{|HH|^2}{\sigma_l(1-|\rho_l|^2)} - \frac{|HV|^2}{\sigma_l\epsilon_l} - \frac{|VV|^2}{\sigma_l\gamma_l(1-|\rho_l|^2)} + 2\frac{Re(HHVV^*\rho_l)}{\sigma_l\sqrt{\gamma_l}(1-|\rho_l|^2)} - \log(\sigma_l^3\epsilon_l\gamma_l(1-|\rho_l|^2))\right\} \quad (4)$$

Regions of the radar image can be completely characterized by the parameters of the covariance matrix. These parameters can be selected using a supervised, semi-supervised, or unsupervised method. A clustering routine on an appropriately selected feature vector can be used for the unsupervised selection of each region's parameters. The problems with this scheme are the computational cost of the clustering technique, performance variation across images, and the need to fine-tune the cluster parameters. In the semi-supervised scheme, the operator specifies the possible number of cluster centers. Thereafter, an iterative algorithm, which alternately splits the training data into the specified number of classes and then computes their cluster centers, is used to find the best possible cluster centers from the training data. Both these methods suffer from the drawback that the resulting cluster centers do not necessarily represent the polarimetric characteristics of actual regions like vegetation, roads, shadows, etc. The supervised method requires training areas and some knowledge of the ground truth. Although the segmentation results are sensitive to the selected training areas, this method is not very restrictive since, during a particular data collection run, we can assume that the characteristics of the various classes are reasonably stationary. The covariance matrix parameters for each region are estimated by obtaining their ML estimate over a set of data points which are known to belong to that region.

It is assumed that as we move a sliding window of size N_s across the entire image, the region label within the window remains the same. The joint distribution of the polarimetric vectors of a small neighborhood set, N_s, of s is considered, to improve classification accuracy. The spatial correlation between the polarimetric vectors of N_s is neglected at the cost of a slight reduction in segmentation accuracy, but with a significant saving in computational cost. The interaction between neighboring pixels is taken into account by the Markov Random Field model. Under the uncorrelated assumption, the conditional distribution of the entire polarimetric data array X, given the label array L is :

$$p(X/L) = \prod_s p(X_s/L_s) \quad (5)$$

and the conditional distribution of the measurement vector at each pixel is

$$p(X_s/L_s = l) = \prod_{i\epsilon N_s} p(X_i/l_i = l) \quad (6)$$

Using a Gibbs representation of (6), we have

$$p(X_s/L_s = l) = \frac{\exp\{-NU_1^s(X_s/L_s = l)\}}{\pi^{3N}} \quad (7)$$

where the energy function U_1^s is

$$U_1^s(X_s/L_s = l) = \frac{|HH^N|^2}{\sigma_l(1-|\rho_l|^2)} + \frac{|HV^N|^2}{\sigma_l\epsilon_l} + \frac{|VV^N|^2}{\sigma_l\gamma_l(1-|\rho_l|^2)} - 2\frac{Re(HH^NVV^{*N}\rho_l)}{\sigma_l\sqrt{\gamma_l}(1-|\rho_l|^2)} + \log(\sigma_l^3\epsilon_l\gamma_l(1-|\rho_l|^2)) \quad (8)$$

and

$$HH^N VV^{*N} = \frac{1}{N}\sum_{i=1}^{N} HH_i VV_i^*; \qquad |HH^N|^2 = \frac{1}{N}\sum_{i=1}^{N} |HH_i|^2 \tag{9}$$

The ML approach to region labeling involves maximization of the LHS of equation (7). This is equivalent to assigning that label to a particular pixel which minimizes the energy function of equation (8). Since the ML approach assigns equal prior probability to each region, the result may appear noisy and pixels in the same region may be left unconnected. The resulting segmentation can be made smoother by incorporating spatial interactions into this model.

2.2 Maximum A Posteriori Estimation of Region Labels

The MRF model is used to describe the spatial interaction between neighboring pixels. According to this model, the conditional distribution of the region label L_s, given the region labels elsewhere, depends only on the labels of an immediate neighborhood, and is given by :

$$p(L_s = l/L_r; r \in N_s^0) = \frac{1}{Z_2}\exp\{-NU_2^s(L_s = l/L_r; r \in N_s^0)\} \tag{10}$$

where the Gibbs energy function U_2^s is :

$$U_2^s(L_s = l/L_r; r \in N_s^0) = -\frac{\beta}{N}\sum_{r \in N_s} \delta_k(L_s - L_r) \tag{11}$$

β is a positive constant which was empirically chosen between [1.0-1.6], [19], independent of the data set, for good segmentation accuracy. $\beta = 0$ corresponds to the ML estimate and a large β leads to excessive smoothing. N_s^0 is a neighborhood of s, of N elements, excluding s and δ_k is the Kronecker delta. Z_2 is a positive normalizing constant, independent of l. N_s^0 is chosen to be the same as N_s for consistency.

The posterior distribution of region label L_s given the single look polarimetric vector X_s and the region labels L_r of the neighborhood is (since X_s and L_r are independent) :

$$p(L_s = l/L_r; r \in N_s^0, X_s) = \frac{p(L_s = l/L_r; r \in N_s^0)p(X_s/L_s = l)}{p(X_s)} \tag{12}$$

Since X_s is known, $p(X_s)$ is just a constant and :

$$p(L_s = l/L_r; r \in N_s^0, X_s) \propto \exp\{-NU_1^s(X_s/L_s = l) - NU_2^s(L_s = l/L_r; r \in N_s^0)\} \tag{13}$$

The posterior distribution of the entire label array, given the entire polarimetric data array is :

$$p(L/X) \propto \exp\{-N\sum_s [U_1^s(X_s/L_s = l) + U_2^s(L_s = l/L_r; r \in N_s^0)]\} \tag{14}$$

The MAP estimate corresponds to the minimization of the MAP energy function :

$$E_{MAP} = \sum_s [U_1^s(X_s/L_s = l) + U_2^s(L_s = l/L_r; r \in N_s^0)] \tag{15}$$

This is a non-convex function which can be minimized by using the simulated annealing [8] algorithm. Other approximate techniques such as iterated conditional mode [2] and maximum posterior marginal [15] can also be used. We have used the iterated conditional mode technique [14].

Figures 1 (a) and (b) show two SAR images with cultural features like buildings, roads, fields, etc. The result of ML and MAP segmentation are shown in Figures 2 and 3. The images in (a) have been segmented into 4 regions, while the ones in (b) have been segmented into 5 regions.

3 CFAR Processing for Man-made Feature Detection

Target detection in SAR images can be done by comparing the received backscatter intensity to a fixed threshold, if only thermal noise is present. But if the target is embedded in spatially varying background clutter, as is common in SAR terrain imagery, an adaptive threshold has to be used to keep the probability of false alarm, a constant. CFAR techniques are useful for detecting metallic objects and other strong reflectors like vehicles, power-line towers, metal guard rails on bridges, etc. The adaptive threshold, with which the output of each pixel is compared, is generated using a weighted combination of the outputs obtained from a moving window of reference cells from the background. The background clutter is assumed to have an underlying statistical distribution. The reference cells are used to obtain estimates of the parameters of the underlying statistical distribution of the clutter.

The traditional circular Gaussian assumption for complex backscatter, which results in a Rayleigh magnitude distribution, is not a good fit for data obtained at low grazing angles and from high resolution radars [23]. Moreover, in order to ensure that the presence of an extended target does not affect the threshold computation, the reference cells must be spatially well separated from the test cell. This tends to make the empirical distribution of the reference cells more spiky than predicted by the Rayleigh magnitude distribution. Distributions with larger tails and larger standard deviation-to-mean ratio, than Rayleigh, seem to match the empirical distribution better. The Lognormal, Weibull and K-distributions satisfy these conditions, but the Lognormal distribution tends to overestimate the range of variation obtained from real clutter. Thus, the Weibull and K-distributions are of interest for clutter modeling, because they lie between the two extremes of Rayleigh and Lognormal, and they include the Rayleigh distribution as a special case.

Several types of CFAR techniques have been suggested in the literature [7, 10, 26, 20, 25, 18], based on the method of obtaining the adaptive threshold from the reference window. The Cell Averaged CFAR (CA CFAR) is the simplest of these, where all cells in the reference window are used to compute the clutter parameters, and hence, the adaptive threshold. The CA CFAR technique assumes that the cell under test is the only possible target while the reference cells are purely clutter. This detector does not perform very well when the reference window overlaps with parts of the same extended target or other targets, interfering with the computation of the threshold. In an Order Statistic CFAR (OS CFAR) detector, an order statistic of the reference cell outputs is used to compute the threshold. The OS CFAR technique works better in extended/multiple target situations because a suitably chosen order statistic is more robust in the presence of additional targets. Other CFAR techniques, such as Greatest of CFAR and Censored CFAR, do not offer significant advantages over the OS CFAR technique for the types of images we are using. In [16] and [17], polarimetric data has been combined into a single channel prior to applying a two-parameter CFAR, but we restrict our attention here to single polarization CFAR processors.

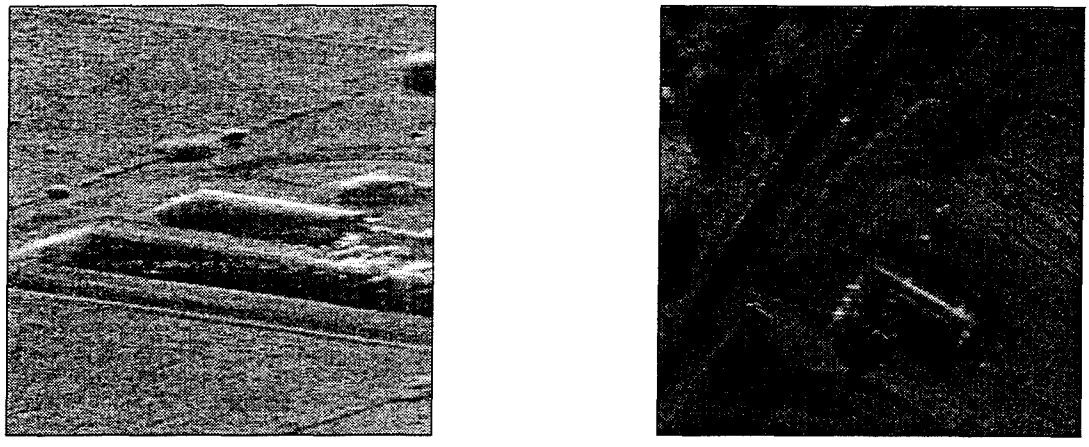

(a) (b)

Figure 1: Original SAR image with buildings and roads

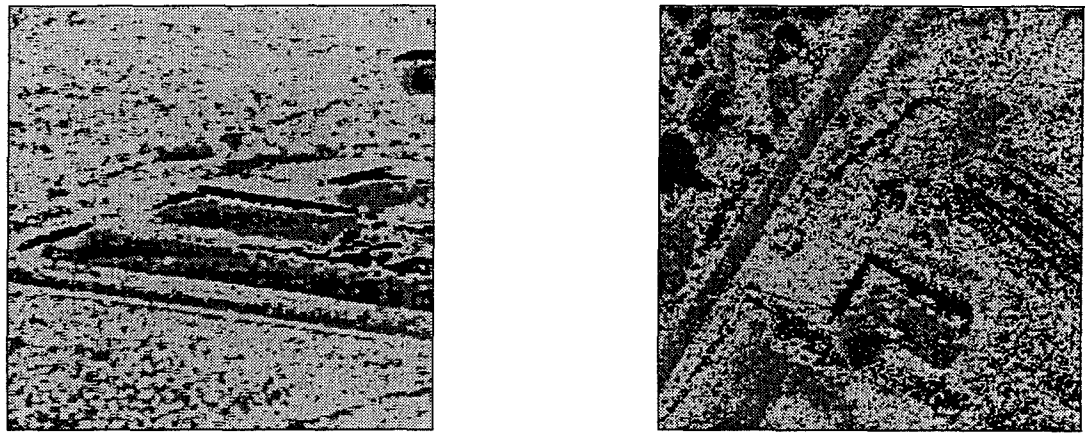

(a) (b)

Figure 2: Result of ML region labeling

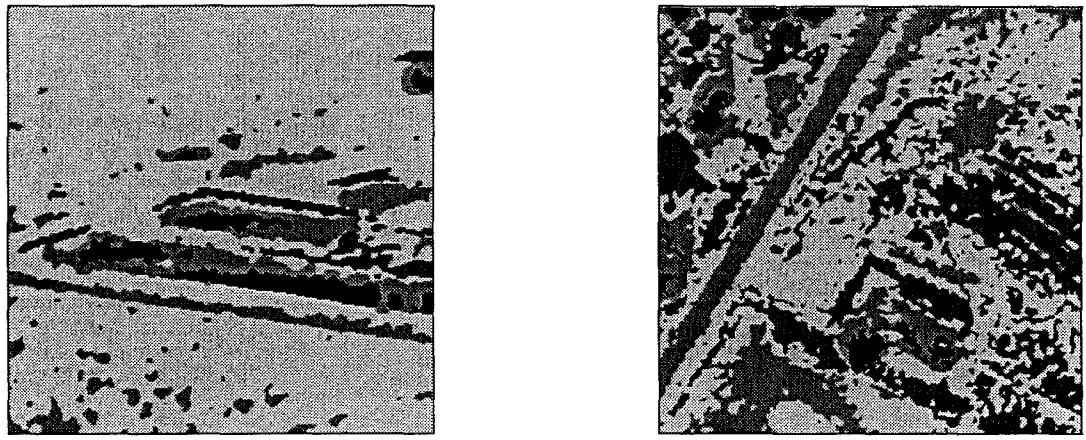

(a) (b)

Figure 3: Result of MAP region labeling

3.1 CFAR Detection in Non-Gaussian Clutter

Under the assumption that the radar backscatter is the result of the superposition of several independent, identically distributed scatterers, the in-phase and quadrature components of the clutter returns become jointly Gaussian processes, as a consequence of the Central Limit Theorem [9]. The resulting backscatter magnitude (intensity) is Rayleigh (exponentially) distributed. Several CFAR processors for this distribution have been derived in the literature [7, 20]. As mentioned before, empirical clutter magnitude distributions for high resolution radars lie between Rayleigh and log-normal in terms of spikiness. The Weibull and K distributions satisfy this requirement and also include the Rayleigh magnitude distribution as a special case.

In a CFAR detector, the voltage in the cell under test is compared with an adaptive threshold derived from a moving window of reference cells from the background. CFAR processing can be posed as a binary hypothesis testing problem :

$$\begin{aligned} H_0 &: \text{Target absent (clutter only)} \\ H_1 &: \text{Target present} \end{aligned}$$

with the decision criterion

$$\pi_0 \underset{H_0}{\overset{H_1}{\gtrless}} \tau z \tag{16}$$

where π_0 is the detector output for the cell under test, z is the test statistic derived from the outputs of the M cells in the reference window, and τ is the adaptive threshold multiplier.

In the general case, given a test statistic Z, with pdf $f_Z(z)$, the probability of false alarm, P_{FA}, and the threshold multiplier, τ, are related by

$$P_{FA} = \int_0^\infty Pr_0[\pi_0 \geq \tau z] f_Z(z) dz \tag{17}$$

where π_0 is the detector output for cell under test, and $Pr_0[.]$ is the probability under the null hypothesis.

The test statistic for the CA CFAR detector is the average of the voltages from all the reference cells. The resulting pdf is the N-fold convolution of the pdf of a single cell. For the OS CFAR processor (based on a single ranked sample), the test statistic is the kth order statistic from M reference cells. The pdf of the kth order statistic is [4]

$$F_k(u) = k \binom{M}{k} f_0(u) F_0(u)^{k-1} [1 - F_0(u)]^{M-k} \tag{18}$$

where $F_0(.)$ and $f_0(.)$ are the univariate clutter-only cumulative distribution function (cdf) and pdf respectively (under the null hypothesis).

3.2 Weibull Clutter

The Weibull model has been suggested for sea and ground clutter magnitude at high resolutions and low grazing angles [21, 22]. The output of the magnitude detector is modeled by the Weibull

pdf

$$f_X(x) = \frac{Cx^{C-1}}{B^C} \exp\left[-\left(\frac{x}{B}\right)^C\right] U(x) \tag{19}$$

where B is the *scale* parameter, C is the *shape* parameter, and $U(x)$ is the unit step function. The scale parameter is related to the average clutter power, P_0 by

$$P_0 = B^2\Gamma\left(1 + \frac{2}{C}\right) \tag{20}$$

where $\Gamma(.)$ is the Eulerian gamma function. The Rayleigh distribution is a special case of this two-parameter distribution, with $C = 2$. Of particular interest to us are Weibull densities with shape parameter values between 1 and 2, i.e., between the exponential and Rayleigh densities. If the shape parameter is known *a priori*, there is a simple expression for the adaptive threshold for the OS CFAR processor with a single ranked sample [13]. Generally, when both the shape and the scale parameter are unknown, there is a need to estimate them simultaneously. Dubey [6] and Cohen [3] derived estimators for the Weibull parameters based on rank-order statistics and an iterative solution to the ML equation, respectively.

The ML CFAR [18] uses the solution of the iterative ML equation to estimate the shape parameter and obtains the scale parameter from this estimate. The following set of equations are used to estimate B and C in [3] (the estimates are denoted as $\hat{B}$ and $\hat{C}$ respectively):

$$\frac{\sum_{m=1}^{M} x_m^{\hat{C}} \ln x_m}{\sum_{m=1}^{M} x_m^{\hat{C}}} - \frac{1}{M}\sum_{m=1}^{M} \ln x_m = \frac{1}{\hat{C}} \tag{21}$$

$$\hat{B} = \left(\frac{1}{M}\sum_{m=1}^{M} x_m^{\hat{C}}\right)^{1/\hat{C}} \tag{22}$$

where M is the number of reference cells considered for estimation and x_m is the output of the mth reference cell. The resulting adaptive threshold, T_{ca}, and the probability of false alarm, P_{FA}, are related by

$$P_{FA} = \exp\left[-\left(\frac{T_{ca}}{\hat{B}}\right)^{\hat{C}}\right] \tag{23}$$

Under Weibull intensity assumption about the backscatter, with unknown shape and scale parameters, [25] describes a CFAR algorithm, based on two ranked samples from the output of a square-law detector. The adaptive CFAR threshold is given by

$$T = y_i^{1-\beta} y_j^{\beta} \tag{24}$$

where y_i and y_j $(i < j)$ are the rank-ordered square-law detected outputs from the background clutter and β is a function of i, j, and the P_{FA}. Since a random variable generated by squaring a Weibull distributed random variable, is itself Weibull distributed with different parameters, and since the CFAR threshold is independent of the distribution parameters, (24) is also applicable to the threshold, τ, corresponding to clutter magnitudes x_i and x_j :

$$\tau = x_i^{1-\beta} x_j^{\beta} \tag{25}$$

Dubey [6] derived an estimator, $\hat{C}$, of the shape parameter based on two ordered samples from a set of Weibull magnitudes :

$$\hat{C} = \frac{\ln[-\ln(1-h_j)] - \ln[-\ln(1-h_i)]}{\ln x_j - \ln x_i} \tag{26}$$

where $h_k = k/(M+1)$ and M is the total number of samples. Dubey showed that the smallest variance for this estimate was obtained when $h_i = 0.1673$ and $h_j = 0.9737$. The corresponding values of i and j are used in (25).

The exact integral relation between β in (25) and P_{FA} was derived in [25] using the joint density of the ith and jth ordered samples, and is given by

$$\begin{aligned} P_{FA} \;=\; & \frac{M!}{(i-1)!(j-i-1)!(M-j)!} \int_{v=0}^{\infty}\int_{u=0}^{\infty} \exp\left[-u^{1-\beta}v^{\beta}\right] [1-\exp(-u)]^{i-1} \\ & \exp(-u)\,[\exp(-v)]^{M-j+1}\,[\exp(-u)-\exp(-v)]^{j-i-1}\,U(v-u)dudv \end{aligned} \tag{27}$$

Levanon and Shor [13] gave an approximate expression for β in terms of the parameter α_i:

$$\beta = \frac{\ln \alpha_i}{\ln\left[-\ln(1-h_j)\right] - \ln\left[-\ln(1-h_i)\right]} \tag{28}$$

where α_i is the scale factor of the OS CFAR for exponential magnitude [20], and is related to the false alarm probability by

$$P_{FA} = \frac{M!(\alpha_i + M - i)!}{(M-i)!(\alpha_i + M)!} \tag{29}$$

The discrepancy between the actual and approximate expressions decreases with increasing false alarm probability. The approximate expression is easier to handle computationally and we have used it in our experiments. Figure 4 shows an HH polarization SAR image of a highway over-pass. The result of Weibull CFAR processing with a $P_{FA} = 10^{-3}$ applied to this image are shown in Figures 5 and 6.

3.3 K-Distributed Clutter

The K distribution has been suggested for experimental sea clutter [24] and ground clutter [27]. The K distribution arises when a complex Gaussian process is modulated by a chi distributed process. Alternately, it can be shown to arise from modulating the power of a Rayleigh magnitude process with a gamma distributed variable. This is the case when the clutter voltage in a given cell exhibits rapid Rayleigh fluctuations, whose mean varies slowly over time according to the gamma distribution. The two parameter K pdf is given by

$$f_X(x) = \frac{4c}{\Gamma(\nu)}(cx)^{\nu} K_{\nu-1}(2cx)\; U(x) \tag{30}$$

where ν is the *shape* parameter, $K_\nu(.)$ is the modified Bessel function of the second kind of order ν, and c is a power parameter related to the mean clutter power, P_0, by $P_0 = \nu/c^2$. When $\nu = \infty$, this reduces to the Rayleigh pdf. The shape parameter controls the spikiness of the clutter, with lower values of ν implying more spiky clutter.

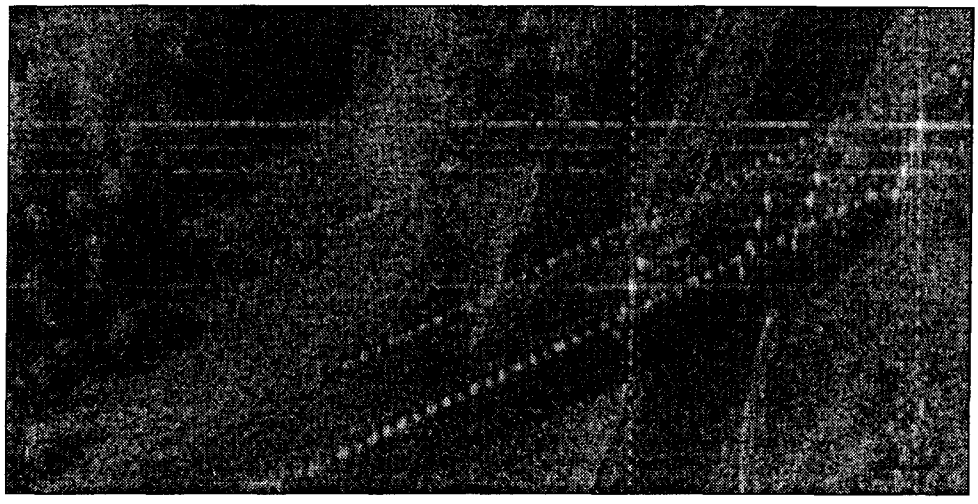

Figure 4: Original *highway overpass* image

For specific values of the shape parameter, namely $\nu = m + 1/2, m = 0, 1, 2, \ldots$, there exist simple expressions for the pdf of the test statistic [1]. Since large values of ν result in the Rayleigh amplitude pdf, and small values give rise to the more spiky clutter that we are interested in, we will restrict our interest to shape parameter values of 0.5 and 1.5.

In general, given the PDF, $p_W(w)$, of the test statistic W, the probability of false alarm is given by [1]

$$P_{FA} = \int_0^\infty \left\{ \frac{2C^\nu}{\Gamma(\nu)} (Tw)^\nu K_\nu(2CTw) \right\} p_W(w) dw \tag{31}$$

For the CA CFAR detector, the test statistic is the sum of M correlated reference cell outputs, each of which is a K-distributed random variable. Closed form expressions (for specific values of ν) for $p_W(w)$ are given in [1]. The resulting PDF for $\nu = 3/2$ is reproduced here as an example

$$p_W(w) = \frac{(2C)^{2M}}{\Gamma(2M)} w^{2M-1} e^{-2Cw} \tag{32}$$

From (18) and (30), the pdf of the kth order statistic of the K distribution is

$$f_Y(y) = 2ck \binom{M}{k} \left[\frac{2(cy)^\nu}{\Gamma(\nu)} \right]^{M-k+1} K_{\nu-1}(2cy) K_\nu^{M-k}(2cy) \left[1 - \frac{2(cy)^\nu}{\Gamma(\nu)} K_\nu(2cy) \right]^{k-1} \tag{33}$$

which can be simplified for $\nu = m + 1/2, m = 0, 1, 2, \ldots$. In particular, for $\nu = 1.5$ we have

$$f_Y(y) = 4c^2 k \binom{M}{k} \exp[-2c(M-k+1)y](1+2cy)^{M-k} \left[1 - (1+2cy)e^{-2cy} \right]^{k-1} \tag{34}$$

Substituting the above expressions for the OS CFAR test statistic pdf in (31) gives the relationships between the probability of false alarm and the adaptive OS CFAR threshold multiplier for $\nu = 1.5$. In general, these equations have to be solved numerically to obtain the appropriate threshold. The result of CFAR processing with a $P_{FA} = 10^{-3}$ and nominal $\nu = 1.5$ applied to the over-pass image of Figure 4 are shown in Figures 7 and 8.

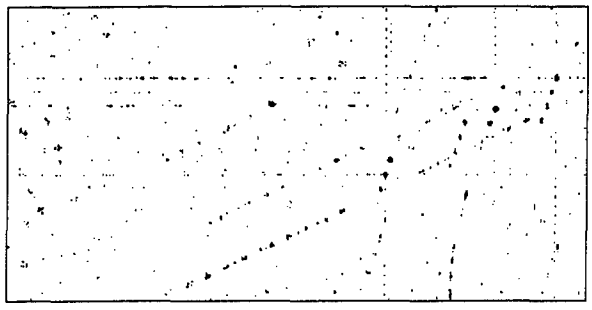

Figure 5: Weibull ML CFAR; $P_{FA} = 10^{-3}$

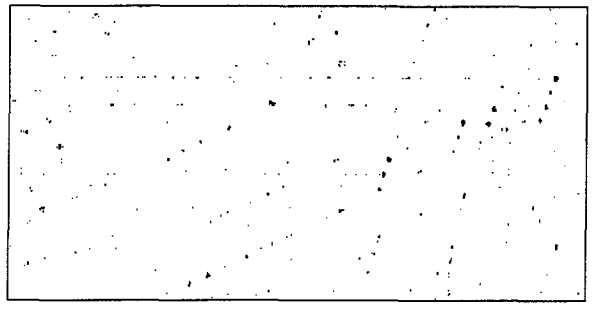

Figure 6: Weibull OS CFAR; $P_{FA} = 10^{-3}$

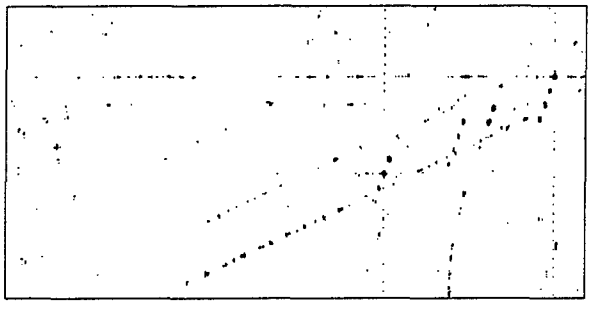

Figure 7: K CA CFAR; $\nu = 1.5$; $P_{FA} = 10^{-3}$

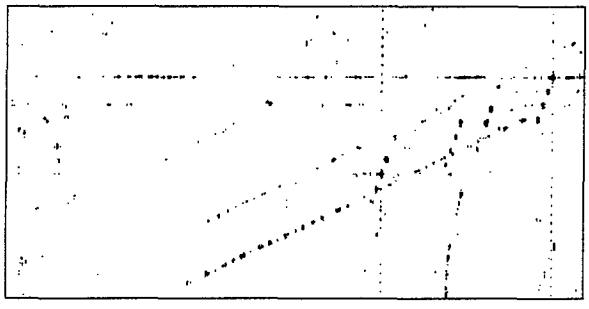

Figure 8: K OS CFAR; $\nu = 1.5$; $P_{FA} = 10^{-3}$

4 Modified Labeling and Site Model Construction

As mentioned earlier, purely statistical segmentation schemes do not perform well in regions containing man-made structures. Several observations can be made about real SAR terrain data. At low to medium depression angles, the vertical walls of buildings, facing the sensor, produce small areas of backscatter. Buildings are, in general, characterized by large shadow regions, bounded by bright L-shaped or linear streaks (cardinal effects) toward the direction of the sensor. These bright streaks often show up as false alarms in target detection algorithms. Also, even when supervised ML segmentation algorithms (with training areas) are used, there is a tendency to misclassify pixels as parts of roads. The fact that roads are ribbon-shaped strips can be used to get rid of most of these false alarms. Similarly, the fact that at high resolutions and low to medium depression angles, trees produce shadows in radar images can be used to reduce misclassification of pixels as trees. Finally, it is difficult to differentiate between shadow regions and calm bodies of water in SAR images, because they produce near-zero backscatter at off-nadir depression angles. Size- , shape- or context-based arguments need to be used to effectively resolve shadows and calm water.

We incorporate these rules and other information about the sensor location, heading and resolution to build an approximate 2D site model of the terrain being imaged. This site model is constructed on the slant range plane. The complete algorithm for the detection of targets, segmentation, and building of a two-dimensional site model from high resolution, polarimetric SAR data is given below. Most of the morphological and other primitive operations mentioned below are described in greater detail in [11].

- **Target detection**
  A two-pass Order Statistic CFAR detector is used for target detection. Non-Rayleigh OS

CFAR detectors are better suited for target detection in high resolution spiky clutter. CFAR detection is initially done independently on the three polarimetric channels, with a low false alarm probability, typically 10^{-3}. The resulting binary images images are logically OR-ed. This conservative approach is suitable for extracting most candidate target pixels from any of the polarization channels. Later, a second CFAR processing step, utilizing a higher false alarm probability (typically 10^{-2}), is performed only in the immediate neighborhoods of previously detected targets. We chose a 5×5 neighborhood around each target pixel detected after the first pass. This two-stage CFAR processing extracts the full extent of large targets, while reducing false alarms.

- **Filtering and streak detection**
  This step is necessary to eliminate isolated false alarms and as a pre-processing routine before building detection. Knowledge about the radar resolution and the approximate size of potential targets can be used to group target pixels into clusters and get rid of isolated pixels. At the same time, if the minimum cluster size is set too large, thin streaks, characteristic of building tops, will be eliminated. We use a 3×3 window, which is moved across the image, retaining groups of at least four pixels. Thereafter, a Hough transform technique is used to detect dominant linear streaks formed by the remaining target pixels. A relative maximum operator is used to detect all the peaks in Hough space, and the corresponding target pixels are passed on to the building detection stage.

- **Supervised ML segmentation**
  Training areas are used to determine the polarimetric covariance matrix parameters of possible terrain classes. We train on nearly homogeneous patches of clearing, grass, road, shadows and trees, obtained from elsewhere in the data sequence. A ML estimate of the region label for each pixel is obtained by maximizing the joint conditional density function of (6), over a local (3×3) neighborhood. Target pixels detected after CFAR processing and subsequent filtering, are not considered in the joint distribution characterization.

- **Building detection**
  Shadows in high resolution SAR terrain images are caused primarily by buildings and trees. Isolated pixels and small regions classified as shadow by the ML segmentation algorithm are eliminated by a morphological erosion operation followed by a dilation operation. The remaining shadow regions are grown using a Euclidean distance criterion on neighboring pixels. Those pixels which border a shadow region, and are *close* to their neighbors (of the shadow class) in terms of the Euclidean distance between their respective intensity measurement vectors, are included in the shadow class. This step is applied repeatedly until there are no further changes in the pixel labels. Finally, those shadow regions which are bounded, to a large extent, by a streak of bright target pixels extending toward the sensor are declared as building shadows.

- **Road extraction**
  Small regions are eliminated and larger ones are filled out using a series of binary morphological dilation/erosion operations on the road regions generated by the ML segmentation step. Bounding rectangles of the appropriate orientation are fitted to the remaining regions, after a connected components algorithm is used to label each region uniquely. Possible ribbon-shaped road segments are detected using appropriate thresholds for the aspect ratio, length and fractional fill of these bounding rectangles. The justification for this step is that road regions are expected to be elongated, nearly rectangular ribbons, and not arbitrarily shaped

blobs. Detected road segments are extended on either side by including previously detected road regions which may have failed the above tests.

- **Modified labeling of natural features**
  ML segmentation is done again for those pixels which were previously misclassified as road or shadow, but this time without including the shadow and road classes. Shadow regions and bodies of water can be resolved at this stage using a size argument, based on the radar depression angle and the approximate height of the tree canopy. Verification of trees is done by eliminating small tree regions and looking for tree shadows (extending away from the sensor) associated with the remaining ones.

- **Re-evaluating target clusters**
  Target streaks corresponding to detected buildings are eliminated from further consideration as possible targets. A filtering step is performed to eliminate isolated target pixels generated by this operation. We use a moving window of size 5×5 to retain only those target clusters which contain at least ten pixels. Bounding rectangles are placed around the remaining target clusters to aid in target recognition and/or facilitate SAR data compression.

The steps in our 2-D site model construction algorithm are shown in Figures 9-10. An original SAR image with moderate urban clutter is shown in Figure 9. Figure 11 shows the possible targets detected after a two-pass CFAR detector, followed by a filtering step to remove isolated target pixels. This result was obtained using an OS CFAR detector for K distributed clutter, with shape parameter $\nu = 1.5$, on each polarization channel, followed by a logical OR operation. The desired false alarm probabilities were chosen to be 10^{-3} and 10^{-2} respectively in each pass. The initial ML segmentation result, with a complex multivariate Gaussian assumption for the backscatter vector, is shown in Figure 12. The target pixels detected after CFAR processing have not been included in the segmentation step. At this stage there are many pixel misclassifications, especially those which are classified as roads and trees. Moreover, no buildings have been detected yet. Figure 12 shows the result of shadow growing followed by building detection. The extracted road is shown in Figure 13, while those tree regions which are supported by the presence of tree shadows extending away from the radar are shown in Figure 14. Finally, Figure 10 shows the complete 2D site model constructed from the polarimetric data. This figure also shows possible target clusters, surrounded by rectangles, which could be used in radar image compression. Figure 15 shows a larger, wide-area SAR image and the result of our site-model building algorithm on this image is shown in 16. Once again, the final segmentation result shows white rectangles placed around possible target clusters.

5 Summary and Conclusions

We have investigated some of the key issues involved in the analysis of SAR images. Our research efforts have resulted in an integrated set of algorithms that can produce annoted 2-D site models of high resolution SAR images. These site models are useful in context based exploitation of SAR images and ATR applications.

Future research issues of interest are: more effective utilization of phase history in polarimetric data, use of interferometric data, and algorithms for registration of SAR images to site models for automatically delineating regions of interest, and fusion of SAR FLIR and IFSAR data for multisensor exploitation using site models.

Figure 9: SAR image with urban clutter

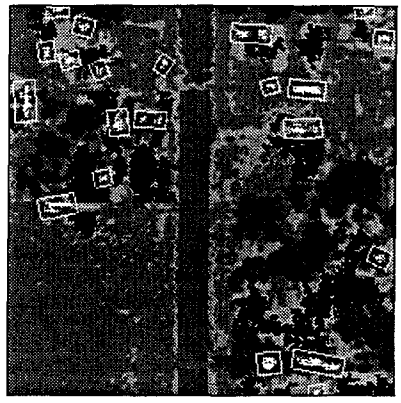

Figure 10: Complete 2D site model

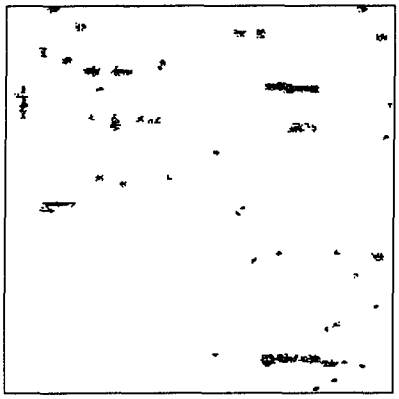

Figure 11: Output of two-pass CFAR

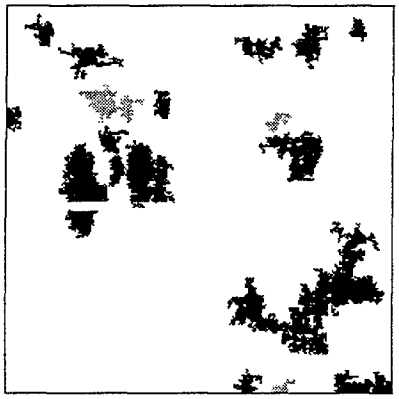

Figure 12: Buildings (gray) & shadows (black)

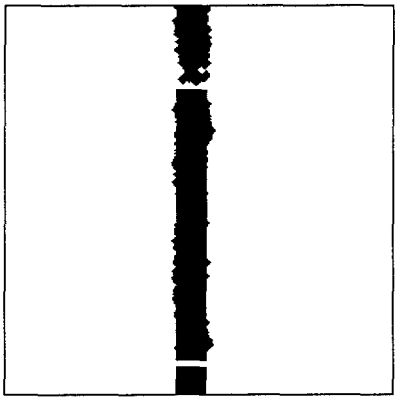

Figure 13: Extracted road

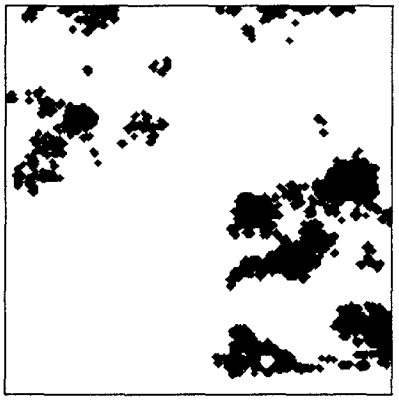

Figure 14: Verified trees

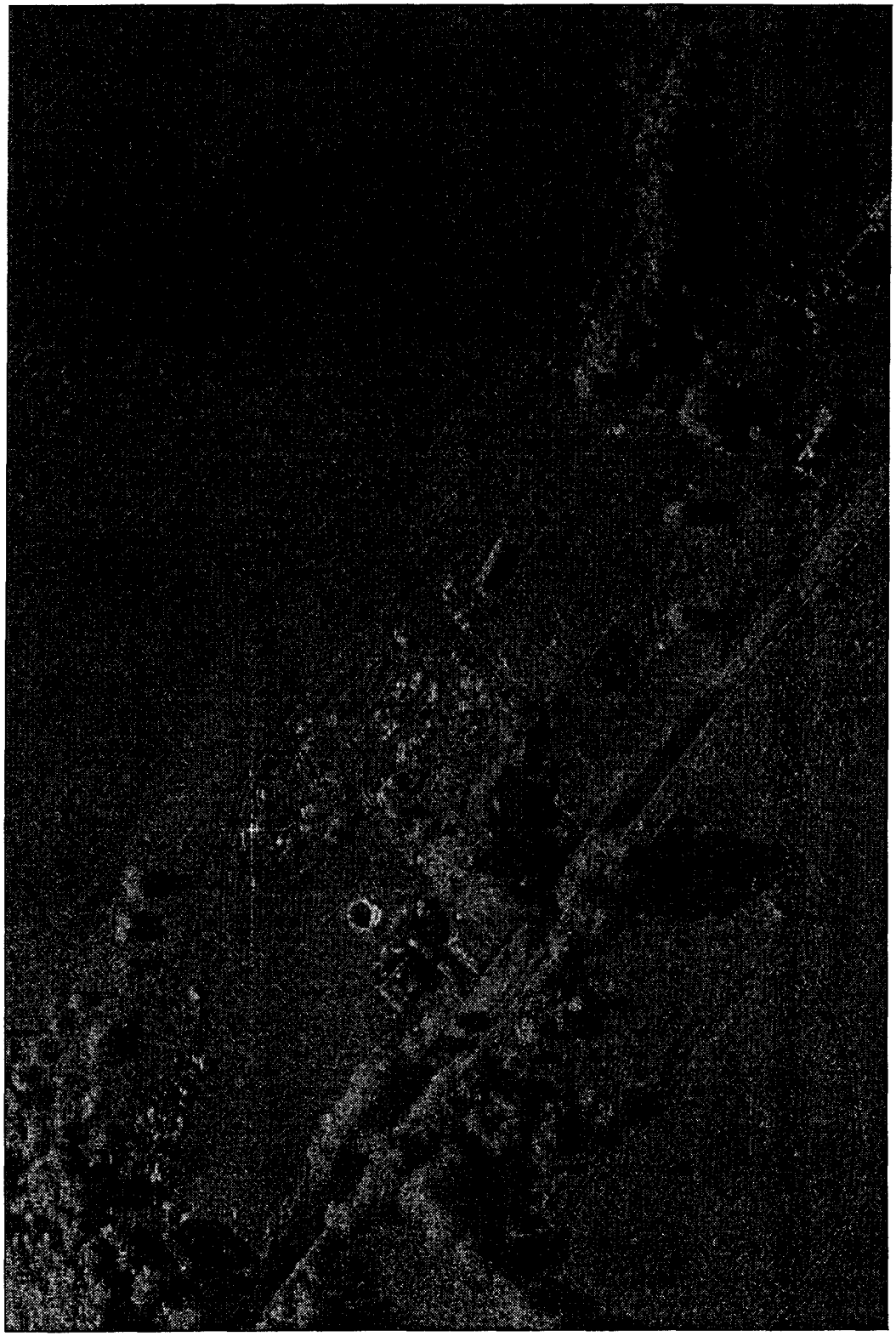

Figure 15: Original wide-area SAR image

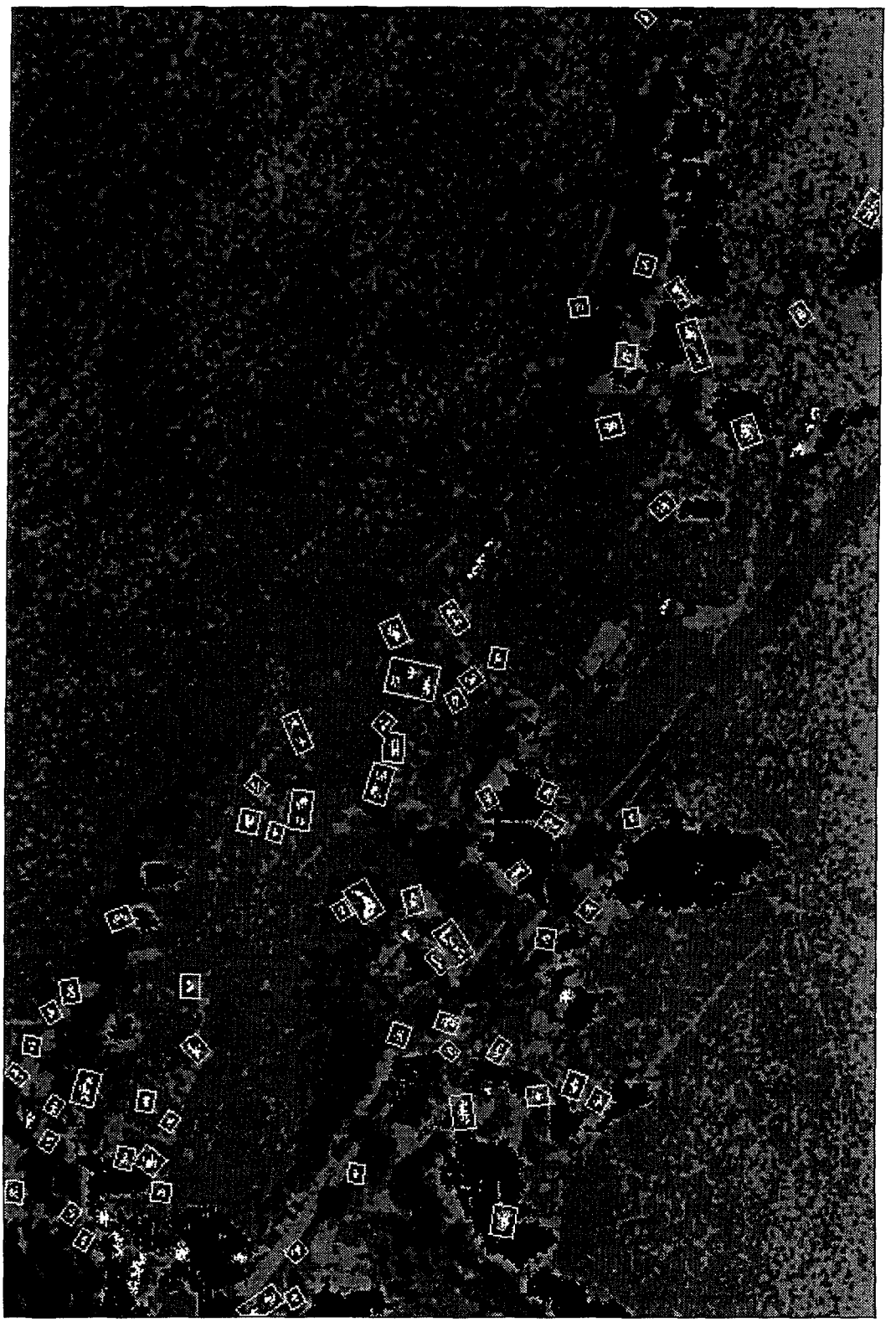

Figure 16: Constructed site-model

References

[1] B. C. Armstrong and H. D. Griffiths. CFAR detection of fluctuating targets in spatially correlated K-distributed clutter. *IEE Proc.-F, Communications, Radar and Signal Processing*, 138(2):139–152, April 1991.

[2] J. Besag. On the statistical analysis of dirty pictures. *J. Royal Statistical Soceity, B*, 48:259–302, March 1986.

[3] A. C. Cohen. Maximum likelihood estimation in the Weibull distribution based on complete and censored samples. *Technometrics*, 7(4):579–588, November 1965.

[4] H. A. David. *Order Statistics.* Wiley, New York, 1981.

[5] H. Derin, P. A. Kelly, G. Vezina, and S. G. Labitt. Modeling and segmentation of speckled images using complex data. *IEEE Trans. Geoscience and Remote Sensing*, 28(1):76–87, January 1990.

[6] S. D. Dubey. Some percentile estimators for Weibull parameters. *Technometrics*, 9(1):119–129, February 1967.

[7] H. M. Finn and R. S. Johnson. Adaptive detection mode with threshold control as a function of spatially sampled clutter-level estimates. *RCA Review*, 29:414–464, September 1968.

[8] S. Geman and D. Geman. Stochastic relaxation, Gibbs distributions, and the Bayesian restoration of images. *IEEE Trans. Pattern Anal. Mach. Intelligence*, PAMI-6:721–741, November 1984.

[9] J. W. Goodman. Some fundamental properties of speckle. *J. Optical Soc. of Am.*, 66(11):1145–1150, November 1976.

[10] V. G. Hansen. Constant false alarm rate processing in search radars. In *Proceedings, IEE Intl. Radar Conf.*, pages 325–332, London, 1973.

[11] H. M. Haralick and L. G. Shapiro. *Computer and Robot Vision*, volume 1. Addison-Wesley, Reading, MA, 1992.

[12] J. A. Kong, A. A. Swartz, H. A. Yueh, L. M. Novak, and R. T. Shin. Identification of terrain cover using the optimum polarimetric classifier. *Journal of Electromagnetic Waves and Applications*, 2(2):171–194, February 1987.

[13] N. Levanon and M. Shor. Order statistic CFAR for Weibull background. *IEE Proc.-F, Communications, Radar and Signal Processing*, 137(3):157–162, June 1990.

[14] B. S. Manjunath, T. Simchony, and R. Chellappa. Stochastic and deterministic networks for texture segmentation. *IEEE Trans. Acoustics, Speech and Signal Processing*, ASSP-38:1039–1049, June 1990.

[15] J. Marroquin, S. Mitter, and T. Poggio. Probabilistic solution of ill-posed problems in computer vision. *J. American Statistical Assoc.*, 82:76–89, 1987.

[16] L. M. Novak, M. C. Burl, W. W. Irving, and G. J. Owirka. Optimal polarimetric processing for enhanced target detection. *Proceedings, IEEE National Telesystems Conf.*, pages 69–75, 1991.

[17] L. M. Novak and S. R. Hesse. On the performance of order-statistics CFAR detectors. *Proceedings, 25th Asilomar Conf. on Signals, Systems. and Computers*, pages 835–840, 1991.

[18] R. Ravid and N. Levanon. Maximum likelihood CFAR for Weibull background. *IEE Proc.-F, Communications, Radar and Signal Processing*, 139(3):256–264, June 1992.

[19] E. Rignot and R. Chellappa. Segmentation of polarimetric Synthetic Aperture Radar data. *IEEE Trans. Image Processing*, 1(3):281–300, July 1992.

[20] H. Rohling. Radar CFAR thresholding in clutter and multiple target situations. *IEEE Trans. on Aerospace and Electronic Systems*, AES-19(4):608–621, July 1983.

[21] D. C. Schleher. Radar detection in Weibull clutter. *IEEE Trans. on Aerospace and Electronic Systems*, AES-12:736–743, November 1976.

[22] M. Sekine, S. Ohtani, T. Musha, T. Irabu, E. Kiuchi, T. Hagisawa, and Y. Tomita. Weibull distributed ground clutter. *IEEE Trans. on Aerospace and Electronic Systems*, AES-17:596–598, July 1981.

[23] M. I. Skolnik. *Introduction to Radar Systems.* McGraw-Hill, New York, 2nd edition, 1980.

[24] K. D. Ward, C. J. Baker, and S. Watts. Maritime surveillance radar part 1: Radar scattering from the ocean surface. *IEE Proc.-F, Communications, Radar and Signal Processing*, 137(2):51–62, April 1990.

[25] P. Weber and S. Haykin. Ordered statistics CFAR for two-parameter distributions with variable skewness. *IEEE Trans. on Aerospace and Electronic Systems*, AES-21:819–821, 1985.

[26] M. Weiss. Analysis of some modified cell-averaging CFAR processors in multiple-target situations. *IEEE Trans. on Aerospace and Electronic Systems*, AES-18(1):102–114, January 1982.

[27] S. H. Yueh, J. A. Kong, J. K. Jao, R. T. Shin, and L. M. Novak. K-distribution and polarimetric terrain radar clutter. *Journal of Electromagnetic Waves and Applications*, 3:747–768, August 1989.